Received: 24 November 2018 | Revised: 10 March 2019 | Accepted: 17 March 2019

DOI: 10.1002/jbio.201800432

FULL ARTICLE

JOURNAL OF BIOPHOTONICS

Nonlinear-optical stain-free stereoimaging of astrocytes and gliovascular interfaces

Aleksandr A. Lanin[1,2] | **Matvei S. Pochechuev**[1,4] | **Artem S. Chebotarev**[1] | **Ilya V. Kelmanson**[5] | **Vsevolod V. Belousov**[5] | **Aleksei M. Zheltikov**[1,2,3,4*]

[1]Physics Department, International Laser Center, M.V. Lomonosov Moscow State University, Moscow, Russia

[2]Russian Quantum Center, Moscow, Russia

[3]Department of Physics and Astronomy, Texas A&M University, College Station, Texas

[4]Kurchatov Institute National Research Center, Moscow, Russia

[5]M.M. Shemyakin and Yu.A. Ovchinnikov Institute of Bioorganic Chemistry, Russian Academy of Sciences, Moscow, Russia

*Correspondence
Aleksei M. Zheltikov, Physics Department, International Laser Center, M.V. Lomonosov Moscow State University, Moscow 119992, Russia.
Email: zheltikov@physics.msu.ru

Funding information
Russian Foundation for Basic Research, Grant/Award Number: 17-00-00212

Abstract

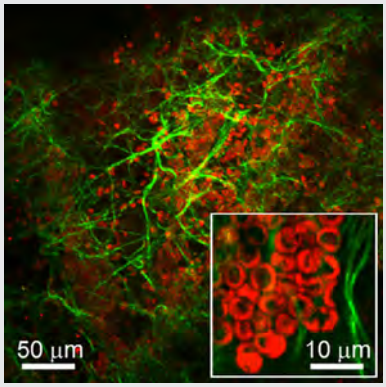

Methods of nonlinear optics provide a vast arsenal of tools for label-free brain imaging, offering a unique combination of chemical specificity, the ability to detect fine morphological features, and an unprecedentedly high, subdiffraction spatial resolution. While these techniques provide a rapidly growing platform for the microscopy of neurons and fine intraneural structures, optical imaging of astroglia still largely relies on filament-protein-antibody staining, subject to limitations and difficulties especially severe in live-brain studies. Once viewed as an ancillary, inert brain scaffold, astroglia are being promoted, as a part of an ongoing paradigm shift in neurosciences, into the role of a key active agent of intercellular communication and information processing, playing a significant role in brain functioning under normal and pathological conditions. Here, we show that methods of nonlinear optics provide a unique resource to address long-standing challenges in label-free astroglia imaging. We demonstrate that, with a suitable beam-focusing geometry and careful driver-pulse compression, microscopy of second-harmonic generation (SHG) can enable a high-resolution label-free imaging of fibrillar structures of astrocytes, most notably astrocyte processes and their endfeet. SHG microscopy of astrocytes is integrated in our approach with nonlinear-optical imaging of red blood cells based on third-harmonic generation (THG) enhanced by a three-photon resonance with the Soret band of hemoglobin. With astroglia and red blood cells providing two physically distinct imaging contrasts in SHG and THG channels, a parallel detection of the second and third harmonics enables a high-contrast, high-resolution, stain-free stereoimaging of gliovascular interfaces in the central nervous system. Transverse scans of the second and third harmonics are shown to resolve an ultrafine texture of blood-vessel walls and astrocyte-process endfeet on gliovascular interfaces with a spatial resolution within 1 μm at focusing depths up to 20 μm inside a brain.

KEYWORDS
astrocytes, label-free microscopy, nonlinear-optical microscopy

1 | INTRODUCTION

For more than a century [1, 2], astroglia have been considered as purely supporting, satellite cells, serving as a sort of brain glue, helping provide a suitable environment within which neurons can execute their diversified functions. This view of astroglia, including, most notably, astrocytes, has, however, drastically changed within the past two decades [3–6], when many remarkable and often surprising properties and functions of astrocytic glia have been discovered. While many of their functions are yet to be understood, astrocytes are currently viewed as critical elements involved in all the key processes behind brain development, function and disease [7, 8]. The role of astrocytic glia has been shown to extend way beyond a metabolic and structural support for neurons, as these cells were found to contribute to a vast range of brain functions under normal and pathological conditions [9, 10]. Specifically, astrocytes have been shown to provide cellular links to neurons, generate important regulatory signals and bridge structures, control synapse formation and function, regulate neurogenesis and brain wiring, as well as modulate neural excitation and inhibition [11–14].

Methods of optical imaging are central to in-depth quantitative studies of the diversified functions and architecture of astroglia. The existing techniques of astroglia imaging [15–17], which largely rely on staining with antibodies to intermediate filament proteins, such as glial fibrillary acidic protein (GFAP) and vimentin, are indispensable in providing important structural information on astroglia, but are inevitably subject to limitations and difficulties, especially severe in live-brain studies. Here, we show that methods of nonlinear optics provide a unique resource to address long-standing challenges in label-free astroglia imaging. Within the past years, methods of nonlinear optics have been providing a rapidly growing platform for label-free brain imaging [18–30], offering a unique combination of chemical specificity [24, 25, 27], the ability to detect fine morphological details [19–21, 26–28] and an unprecedentedly high, subdiffraction spatial resolution [29, 30]. Second-harmonic generation (SHG) has gained a broad acceptance as a tool for the microscopy of noncentrosymmetric molecules and brain structures [18, 19]. Third-harmonic-generation (THG), on the other hand, does not require central symmetry breaking, yielding a useful nonlinear signal from both cell surfaces, as well as inter- and intracellular optical inhomogeneities [20–23, 26, 28]. Integration of SHG and THG has been shown to open new routes in multimode brain microscopy [27]. Still, with the SHG channel almost exclusively reserved for collagen imaging, the full potential of such multimodal nonlinear-optical brain imaging is far from being fully realized.

In experiments presented below in this paper, we show that, with a suitable beam-focusing geometry, SHG microscopy can be extended to a high-resolution label-free imaging of fibrillar structures of astrocytes, most notably astrocyte processes and their endfeet. Moreover, with the laser wavelength tuned to a three-photon resonance with the Soret band of hemoglobin, SHG imaging of astrocytes can be implemented in parallel with a resonance-enhanced THG imaging of red blood cells. With astroglia and red blood cells providing two physically distinct imaging contrasts in SHG and THG channels, a parallel detection of the second- and third-harmonic signals, as experiments presented in this paper show, enables a high-contrast, cell-specific stereoimaging of gliovascular interfaces in the brain of living animal models, thus offering a unique resource for in-depth research into astroglia and their most important functions within the central nervous system (CNS).

2 | EXPERIMENTAL

2.1 | Laser microscope

An optical system used in our experiments (Figure 1) consists of a laser source of ultrashort frequency-tunable near-infrared pulses and an upright microscope. The laser source comprises a short-pulse Ti: sapphire master oscillator and an optical parametric oscillator (OPO). The Ti: sapphire laser oscillator delivers transform-limited pulses with a pulse width of about 90 fs, a central wavelength tunable from ≈700 to 980 nm, and an energy up to 40 nJ at a pulse repetition rate of 76 MHz. These pulses provide a pump for the OPO, based on a periodically poled potassium titanyl phosphate crystal, which produces a chirped-pulse output tunable within the range of wavelengths λ_0 from ≈1000 to 1550 nm, with the output pulse width varying within this tunability range from ≈350 to 500 fs. The output pulse energy at the center of the OPO tunability range is about 8 nJ. The chirped-pulse OPO output is carefully compressed to a ≈90-fs transform-limited pulse width with a home-built prism pulse compressor, providing an energy throughput above 80%.

The compressed-pulse OPO output is focused into a brain slice with a water-immersion XLUMPlanFLN 20×

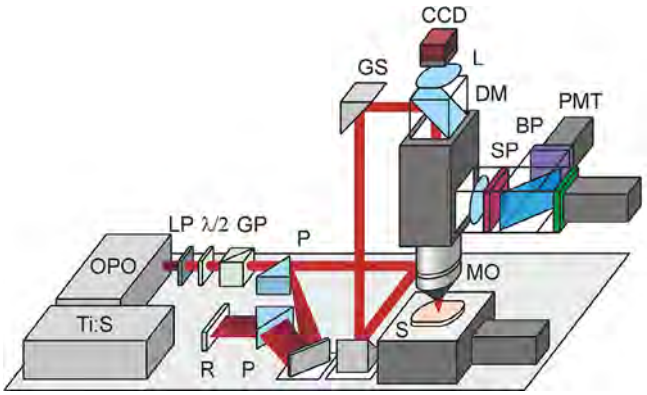

FIGURE 1 Laser setup for multiplexed nonlinear-optical stereoimaging: Ti: S, titanium sapphire laser oscillator; OPO, optical parametric oscillator; λ/2, half-wave plate; GP, Glan-Taylor prism, DM, dichroic mirror; LP, long-pass filter; SP, short-pass filter; BP, bandpass filter; P, prism; R, roof mirror L, lens; CCD, CCD camera; GS, galvoscanner module; MO, microscope objective; S, sample; PMT, photomultiplier tube

NA = 1.00 near-infrared (near-IR) objective in an upright-microscopy scheme. The second and third harmonics of the focused near-IR laser beam are collected by microscope objectives in both transmission and epi-detection geometries to be detected with an H7422PA-40 photomultiplier. Signal readout and acquisition were controlled by an in-house software. The second- and third-harmonic signals are acquired simultaneously. To this end, the second harmonic is separated from the third harmonic by a dichroic mirror with a cutoff at ≈505 nm. The second harmonic is then transmitted through a bandpass filter with a transmission band of ≈40 nm centered at 650 nm. The third harmonic is filtered with the use of a bandpass filter with a transmission band of ≈17 nm centered at 434 nm. All the images presented below in this paper are recorded in the epi-detection geometry.

2.2 | Brain samples

Brain slice samples studied in experiments were extracted from 12-week-old Wistar-line healthy male rats. The samples were fixed in 4% paraformaldehyde solution in protein-free phosphate-buffered saline (PBS). Imaging experiments were performed on ≈10-mm-thick brain slices within 2 to 15 hours following fixation. In our experiments, we focus on astrocytes—perhaps, the most structurally and functionally prominent astroglial cells. As one of their important functions within the CNS, astrocytes play an active role in the formation of the blood-brain barrier (BBB) [13, 31–33], regulating the formation of endothelial tight junctions, modulating transporter expression and promoting specialized enzyme functions. Organized into gliovascular units, astrocytes connect to local segments of blood vessels, interacting with their endothelial cells through the endfeet of their processes, which often form a continuous interface layer around microvessels and brain capillaries [13, 31–33].

2.3 | Beam focusing and pulse-chirp compensation

As the OPO output is tuned to different radiation wavelengths, the signal beam waist inside the OPO is slightly shifted. The resulting problem is manifold. First, this beam-waist displacement gives rise to an uncompensated chirp, stretching the OPO output and this, lowering the efficiency of second- and third harmonic generation, as well as the efficiency of two-photon excitation—nonlinear-optical processes used for microscopy in our experiments. Moreover, when focused to a small beam size by a microscope objective, longer laser pulses tend to increase the risk of a broad class of unwanted, potentially damaging nonlinear photoprocesses in a biological system [34, 35]. Second, a varying signal-beam-waist location inside the OPO translates into a shift of the focused beam inside a brain sample, which becomes a function of the OPO output wavelength, thus preventing a precise positioning of the imaging beam. Third, as the signal-beam-waist position changes from one OPO wavelength to another, the divergence and beam diameter of the OPO output also become wavelength-dependent. As a consequence, special measures are needed to match the laser beam diameter with the aperture of the microscope objective.

In our experimental system, the adverse effects of a shifting beam waist inside the OPO are dealt with by using carefully designed, independently adjustable and finely tunable systems for chirp compensation and beam-focusing optimization. A home-built system for chirp compensation consists of flint-glass prisms, providing a variable group-velocity dispersion, needed to post-compensate the chirp of OPO output pulses, as well as pre-compensate the chirp introduced by optical components of the microscope down the line. An adjustable telescope is then used to carefully match the laser beam diameter with the aperture of the microscope objective. As a result of these measures, the pulse width of the laser pump in the imaging plane was within less than 10% of the ≈90-fs transform-limited pulse width, with the overall throughput of the entire optical imaging system no worse than 80%. The energy of ≈1305-nm laser pulses in the imaging plane never exceeded 2.8 nJ, corresponding to a peak power at the level of 30 kW and an average power of ≈220 mW.

It should be noted that the problem of a shifting beam waist is common for a broad class of OPO sources used for nonlinear-optical microscopy. The methods of dealing with this problem implemented in our experiment can be

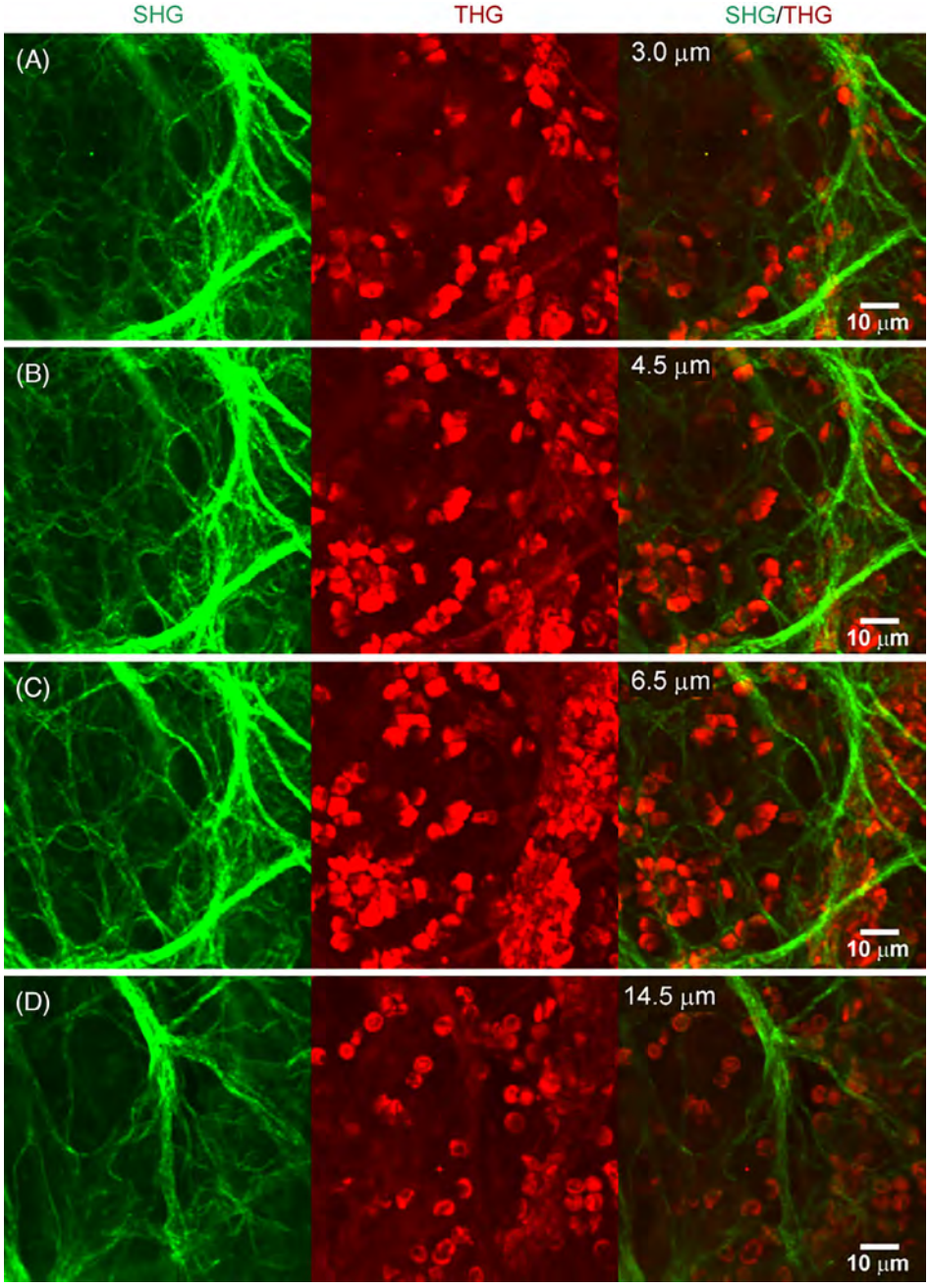

FIGURE 2 A stack of second-harmonic generation/third-harmonic generation images recorded by focusing 90-fs laser pulses with a central wavelength $\lambda_0 \approx 1305$ nm at a depth of $z \approx 3.0$ μm (A), 4.5 μm (B), 6.5 μm (C) and 14.5 μm (D) inside rat's brain. The second- and third-harmonic intensities are encoded by levels of green and red, respectively. The scale bar is 10 μm

therefore regarded as universal recipes for nonlinear microscopy with a higher resolution, higher definition, more precise beam positioning and lower risk of radiation damage in a biological sample.

3 | RESULTS AND DISCUSSION

3.1 | Label-free SHG imaging of astrocytes

Visualizations S1 and S2 and Figures 2A-D present typical stacks of depth-resolved SHG/THG images of the leptomeninx area and the adjacent brain tissue inside rat's brain. This region of brain is of special significance for the analysis of astrocytes and their role in BBB formation and regulation [13]. SHG/THG images in Visualizations S1 and S2 have been taken by scanning the focus of the laser beam up to, respectively, $z = 21.5$ μm and 34 μm inside rat's brain with a 0.5- and 1.0-μm step along the z-axis. No degradation of spatial resolution has been observed within the entire range of depth scan up to $z = 50$ μm. In a separate experiment, the attenuation of the second- and third-harmonic signals was found to follow an exponential behavior with typical attenuation lengths $l_{sh} \approx 370$ μm for the second harmonic and $l_{th} \approx 280$ μm for the third harmonic.

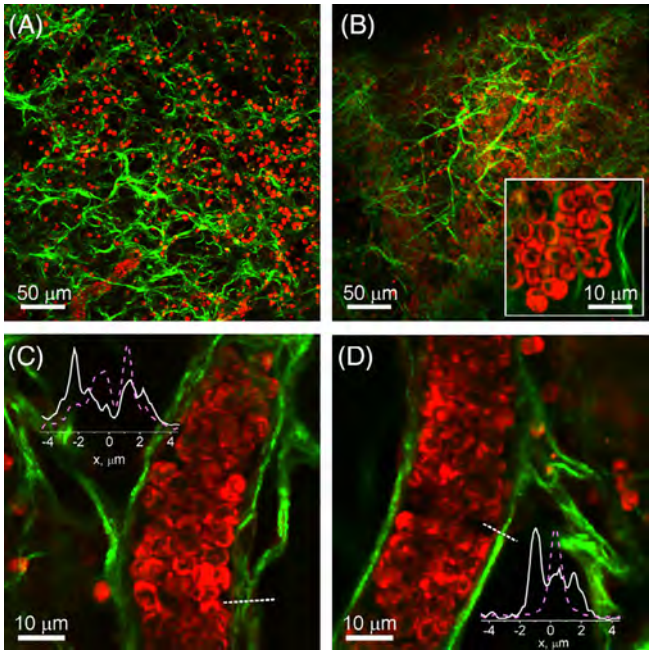

FIGURE 3 Typical second-harmonic generation/third-harmonic generation images recorded by focusing 90-fs laser pulses with a central wavelength $\lambda_0 \approx 1305$ nm at $z \approx 4.0$ μm (A), 9.0 μm (B), 17 μm (C) and 19 μm (D) inside rat's brain. The insets show an enlarged view of a group of red blood cells (B) and transverse scans of the second and third harmonics across a gliovascular interface (C, D)

Due to the second-order optical nonlinearity inherent in glial fibrillary acidic protein in astrocytic processes possess [36], SHG is ideally suited for astroglia imaging. In SHG images in Figures 2A-D, 3A-D and 4A,B, as well as in Visualizations S1 and S2, astrocytes are visible as signature, star-shaped structures with extended, filamentlike processes emanating from their cell bodies. As a typical feature, the astrocytic processes wrap around blood vessels, with their endfeet often completely covering the entire surface of blood-carrying capillaries (Figure 3C, D), providing an interaction path between astrocytes and capillary endothelial cells. The basement membrane surrounding endothelial cells and separating capillaries from astrocytes includes type-IV collagen [13, 31–33], which contributes to the second-harmonic signal.

3.2 | Colocalizing SHG and fluorescence from fluorescent-reporter-labeled astrocytes

For a conclusive verification of the ability of SHG microscopy to detect and image astrocytes, imaging experiments were performed on rat's cortex where astrocytes were stained with a genetically encodable SypHer-2 fluorescent reporter [37]. When placed under the gfa2 promoter within a virus construct [38] and injected into the cortex, SypHer-2 is

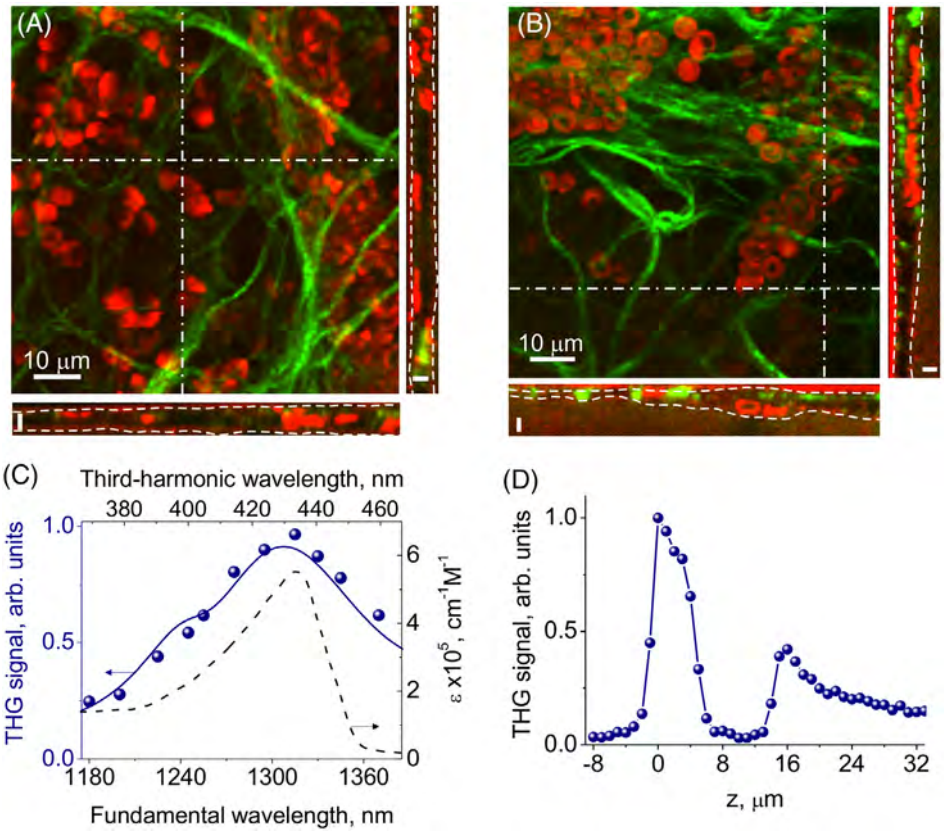

FIGURE 4 A and B, Typical second-harmonic generation/third-harmonic generation images taken at (A) $z \approx 5.5$ μm and (B) 8.0 μm inside rat's brain. The z-resolved SHG/THG images taken as scans along the dash-dotted lines shown in the xy-images are presented as marginals with the boundaries of the arachnoid membrane and pia mater shown by the dashed lines. C, The intensity of the third harmonic measured as a function of the optical parametric oscillator (OPO) output wavelength (filled circles) and the molar extinction ε of Hb (dashed line) versus the driver (lower axis) and third-harmonic (upper axis) wavelength. The solid line shows the third-harmonic intensity as a function of the OPO output wavelength calculated with a full model including the frequency dependences of absorption, refraction, and THG nonlinear susceptibility of Hb. D, The z-scan of the third-harmonic intensity inside rat's brain

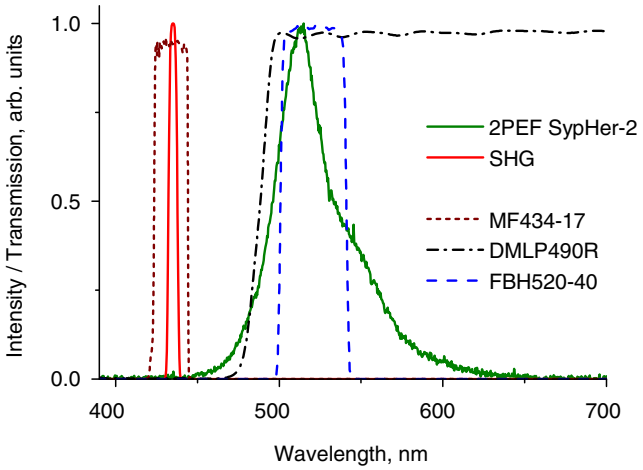

FIGURE 5 The spectra of the second harmonic (red solid line) and two-photon-excited fluorescence of SypHer-2 (green solid line) driven by a 870-nm, approximately 100-fs Ti: sapphire laser output. Also shown are the transmission spectrum of the MF434-17 filter (maroon dotted line), FBH520-40 filter (blue dashed line), and the DMLP490R dichroic mirror (dash-dotted line)

expressed in our experiments in the astrocytes inside rat's cortex. For a verification of SypHer-2 expression in astrocytes, the rats were euthanized after the experiment, the brain was fixed for 24 hours in 4% paraformaldehyde in PBS and sliced into coronal sections. Expression of SypHer-2 was then evaluated in these sections under a fluorescent microscope.

A two-photon excitation of SypHer was provided by a 870-nm, approximately 100-fs Ti: sapphire laser output, yielding a two-photon-excited fluorescence (TPEF) with a spectrum as shown by the green solid line in Figure 5. On the other hand, the spectrum of the signal resulting from SHG, also driven in this experiment by approximately 100-fs, 870-nm Ti: sapphire laser pulses, peaks at ≈435 nm (red solid line in Figure 5). The second harmonic was separated from the TPEF signal with a DMLP490R longpass dichroic mirror with a cut-on wavelength at ≈490 nm (dash-dotted line in Figure 5). The second harmonic and TPEF signals were then transmitted through MF434-17 and FBH520-40 filters in their respective detection channels. The transmission spectra of these filters are shown by the maroon dotted and blue dashed lines in Figure 5. The spectrum of the second harmonic transmitted through the MF434-17 filter is seen to be well-isolated from the SypHer-2 TPEF signal transmitted through the FBH520-40 filter, preventing the TPEF signal from leaking into the second-harmonic detection channel.

A typical TPEF image recorded at a depth of ≈96 μm inside rat's cortex is shown in the left part of Figure 6. The lower signal-to-noise ratio in the second-harmonic channel in this experiment is due to several factors. First, 870-nm laser radiation is more prone to loss and scattering in brain tissues compared to longer-wavelength, ≈1305-nm laser radiation. Second, the second harmonic signal, centered at ≈435 nm, is also subject to a stronger attenuation in brain tissues. Third, the second-harmonic signal has to be collected from a much larger depth in this experiment.

Despite these difficulties, the SypHer-2-expressing astrocytes are clearly visible in this image. The central part of Figure 6 presents an SHG image of the same cortex area. While much of the second-harmonic signal is produced by collagen, in agreement with the existing literature (see, eg, Refs. [18–21], [23–26]), astrocytes are readily identifiable in these images by their characteristic shape. An overlay of the TPEF and SHG images, presented in the right part of Figure 6, confirms spatial colocalization of the TPEF and SHG signals. These findings are fully consistent with the results of the earlier studies [36], where SHG from astrocytes was verified by a colocalization of the second harmonic and signals from three fluorescent sensors—GFAP-specific Cy3-anti-GFAP antibodies, sulforhodamine 101 (SR101) and an Oregon Green calcium indicator.

3.3 | Three-photon resonant enhancement of THG from red blood cells

The intensity of the second harmonic signal in these images was found to show little or no variations when measured as a function of the pump wavelength within the entire OPO output tunability range. On the contrary, the third-harmonic intensity was found to display a broad, yet clearly pronounced maximum centered at around the maximum of the

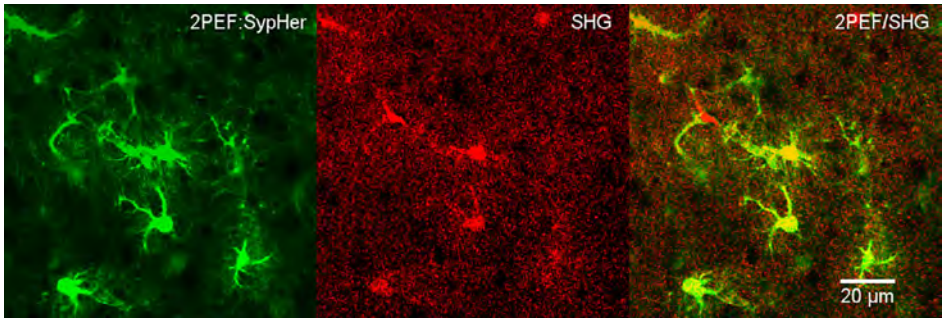

FIGURE 6 Images taken at a depth of ≈96 μm inside rat's cortex using two-photon-excited fluorescence from SypHer-expressing astrocytes (2PEF: SypHer, right) and second-harmonic generation (SHG, middle). An overlay of the TPEF and SHG images (2PEF/SHG) is presented in the right part of the figure

Soret band of hemoglobin (Hb), $\lambda_{TH} \approx \lambda_{Hb} \approx 435$ nm (Figure 4C). This assignment of resonant enhancement observed in THG was verified in a separate experiment performed on individual erythrocyte cells on a glass substrate. With the laser wavelength tuned on the three-photon resonance $\lambda_0 \approx 3\lambda_{Hb} \approx 1305$ nm, the intensity of the third harmonic from rat brain samples studied in our experiments was found to be at least a factor of 4.5 higher than the intensity of an off-resonance third-harmonic signal (Figure 4C).

This resonance enhancement of THG is central for a high-contrast, high-brightness THG imaging of astrocytes and gliovascular interfaces. Specifically, with the laser wavelength set on the three-photon resonance $\lambda_0 \approx 3\lambda_{Hb} \approx 1305$ nm, the arachnoid-membrane and pia-mater boundaries become clearly resolved in the z-scans of the third harmonic (at $z \approx 0$ and $z \approx 15$ μm in Figure 4D). These boundaries are shown by the dashed lines in the z-resolved SHG/THG images, presented as marginals below and to the right of the xy-maps of the second- and third harmonics in Figure 4A, B. The overall thickness of the leptomeninx area and the adjacent brain tissue studied in our experiments is seen to vary from ≈6 to ≈20 μm, reaching its maximum values near blood vessels and veins. Notably, red blood cells, readily visible in Figures 3A-D and 4A, B as bright spots of the third-harmonic signal, cannot penetrate through the tight connections of arachnoid epithelium—one of the key BBB elements, remaining trapped in the studied brain area.

3.4 | The pump wavelength for SHG astrocyte imaging

As show in the previous section, the laser wavelength $\lambda_0 \approx 1305$ nm is advantageous for multiplex nonlinear-optical brain imaging as it provides a three-photon-resonance enhancement of THG from red blood cells. We are going to show now that this wavelength is also in many ways advantageous, if not optimal, for SHG. As a first significant factor, shifting the laser pump to a longer wavelength, compared, as a prominent example, to a standard, ≈800-nm Ti: sapphire laser output, helps reduce scattering as one of the main factors of radiation attenuation in a biological tissue. The $\lambda_0 \approx 1305$ nm wavelength appears to be a reasonable choice in this regard as it provides a very significant decrease in scattering without falling close to strong water absorption bands, such as those observed at around ≈1.44 and 1.92 μm. Finally, as an important technical factor, the second-harmonic wavelength, $\lambda_{SH} = \lambda_0/2$, should lie within the range where the optical elements of the imaging system provide high transmission and high-sensitivity detection is possible. Since with $\lambda_{SH} \approx 660$ nm, the sensitivity of a typical high-performance, high-sensitivity photodetector falls off by approximately 30% relative to its maximum, attainable at ≈570 nm, the choice of the pump wavelength at $\lambda_0 \approx 1305$ nm is also justified from this perspective.

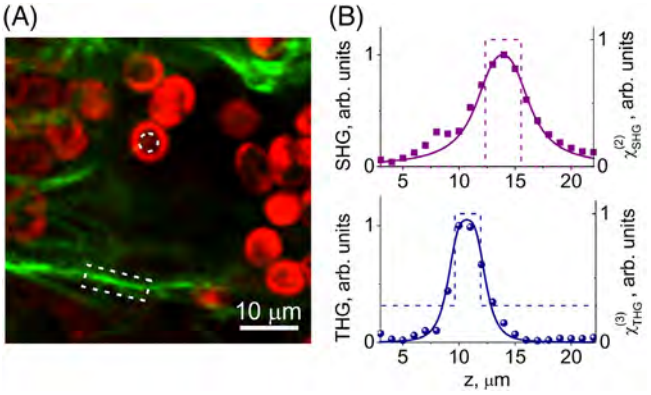

FIGURE 7 A, A typical second-harmonic generation/third-harmonic generation image taken at $z \approx 12.4$ μm inside rat's brain. B, The z-scans of the second (upper plot) and third (lower plot) harmonic: (boxes and circles) experiment, (solid lines) modeling. The z-profiles of $\chi^{(2)}_{SHG}$ and $\chi^{(3)}_{THG}$ providing the best fit for the experimental z-scans are shown by the dashed lines

3.5 | Depth-resolved SHG/THG imaging

In Figure 7, we present a quantitative analysis of a typical z-stack of depth-resolved SHG/THG images of the leptomeninx area and adjacent brain tissues in rat brain (Figures 2A-D, Visualizations S1 and S2). This analysis is based on the full model of SHG and THG in brain [20–22, 26, 28] with astrocyte processes and red blood cells modeled as stepwise changes in SHG and THG nonlinear susceptibilities $\chi^{(2)}_{SHG}$ and $\chi^{(3)}_{THG}$ (shown by dashed lines in Figure 6B). Briefly, the power of the Nth optical harmonic is calculated as

$$P_N(z) = n\varepsilon_0 c\pi w_0^2 |A_N(z)|^2, \quad (1)$$

where $n = n(\lambda)$ is the wavelength-dependent refractive index, ε_0 is the vacuum permittivity, c is the speed of light in vacuum, w_0 is the beam-waist radius, $b = 2\pi n w_0^2/\lambda_0$ is the confocal parameter,

$$A_N(z) = \frac{iN\omega}{2nc}\chi^{(N)}A_1^N J_N(\Delta k, z_0, z), \quad (2)$$

$$J_N(\Delta k, z_0, z) = \int_{z_0}^{z} \frac{\exp\left(i\Delta k z'\right)dz'}{\left(1 + 2i\frac{z'}{b}\right)^{N-1}}, \quad (3)$$

$\chi^{(N)}$ is the Nth order nonlinear-optical susceptibility ($N = 2$ and $\chi^{(N)} = \chi^{(2)}_{SHG}$ for SHG, $N = 3$ and $\chi^{(N)} = \chi^{(3)}_{THG}$ for THG), z_0 and z are the coordinates of the boundaries of the nonlinear medium, and $\Delta k = 2\pi N[n(\lambda_0/N) - n(\lambda_0)]/\lambda_0$ is the wave-vector mismatch for Nth harmonic generation.

The second-order nonlinear susceptibility $\chi^{(2)}_{SHG}$ is set equal to zero outside astrocyte processes (dashed line in Figure 7A, B) as the surrounding brain tissue is assumed to be centrosymmetric. The cubic susceptibility $\chi^{(3)}_{THG}$, on the other hand, is taken nonzero also outside the red blood cells (dashed line in Figure 7A, B) to account for a nonvanishing third-order nonlinearity of the surrounding brain tissue. The confocal parameter b of the laser beam was esimated in a separate test experiment performed on precalibrated polystyrene beads, yielding $b \approx 2.8$ μm. The best fit for the experimental z-scans of the second- and third-harmonic intensity is achieved with a $\chi^{(2)}_{SHG}$ step for an astrocyte process from $z_1 \approx 12.4$ μm to $z_1 + d_a \approx 15.5$ μm (solid purple line in Figure 7B) and a $\chi^{(3)}_{THG}$ step for a red blood cell from $z_2 \approx 9.5$ μm to $z_2 + d_{RBC} \approx 11.7$ μm, providing reasonable estimates for typical sizes of astrocyte processes, d_a, and red blood cells, d_{RBC}.

The insets to Figure 3C, D present the transverse scans (x-scans) of the second and third harmonics measured across a gliovascular interface. Both scans are seen to resolve an ultrafine texture of blood-vessel walls and astrocyte-process endfeet on this interface. The x-scan of the third harmonic in Figure 3D features three well-resolved peaks, visualizing a ≈0.9-μm-thick inner wall of this interface, followed by a ≈1.0-μm-thick central part and a ≈0.9-μm-thick outer wall. The x-scan of the second harmonic, on the other hand, features a single well-resolved, ≈0.9-μm-wide peak whose position correlates very well with the central peak in the x-scan of the third harmonic, corresponding to the central part of this interface, where most of the quadratic nonlinearity of astrocyte processes is localized.

An alternative method of label-free astrocyte imaging could involve endogenous fluorescence. Within the studied range of laser excitation wavelengths, however, we did not find any endogenous fluorescence signal that would be specific to astrocytes and that would be at least in the same order of magnitude as the second-harmonic signal.

4 | CONCLUSION

To summarize, we have demonstrated that SHG microscopy can enable a high-resolution label-free imaging of fibrillar structures of astrocytes, most notably astrocyte processes and their endfeet. SHG microscopy of astrocytes is integrated in our approach with nonlinear-optical imaging of red blood cells based on THG enhanced by a three-photon resonance with the Soret band of hemoglobin. With astroglia and red blood cells providing two physically distinct imaging contrasts in SHG and THG channels, a parallel detection of the second and third harmonics enables a high-contrast, high-resolution, stain-free stereoimaging of gliovascular interfaces in the CNS.

ACKNOWLEDGMENTS

This research was supported in part by the Russian Foundation for Basic Research (project nos. 17-00-00212, 17-00-00214, 18-29-20031, 16-32-60163, 16-29-11799, 18-32-20191) and Welch Foundation (Grant No. A-1801-20180324). Research by A.A.L. and A.S.C. into nonlinear microspectroscopy was supported by the Russian Science Foundation (project no. 18-72-10094). Research by A.M.Z., A.A.L. and M.S.P. into short-pulse sources for nonlinear imaging was supported by the Russian Science Foundation (project no. 17-12-01533).

ORCID

Aleksei M. Zheltikov https://orcid.org/0000-0002-9138-0576

REFERENCES

[1] R. Virchow, *Allg. Zschr. Psychiatr.* **1846**, *3*, 424.
[2] G. G. Somjen, *Glia* **1988**, *1*(2), 2.
[3] F. W. Pfrieger, B. A. Barres, *Science* **1997**, *277*, 1684.
[4] P. G. Haydon, *Nat. Rev. Neurosci.* **2001**, *2*, 185.
[5] E. M. Ullian, S. K. Sapperstein, K. S. Christopherson, B. A. Barres, *Science* **2001**, *291*, 657.
[6] H. Song, C. F. Stevens, F. H. Gage, *Nature* **2002**, *417*, 39.
[7] G.-F. Tian, H. Azmi, T. Takano, Q. Xu, W. Peng, J. Lin, N. Oberheim, N. Lou, X. Wang, H. R. Zielke, *Nat. Med.* **2005**, *11*, 973.
[8] B. A. Barres, *Neuron* **2008**, *60*, 430.
[9] M. Nedergaard, B. Ransom, S. A. Goldman, *Trends Neurosci.* **2003**, *26*, 523.
[10] A. Volterra, J. Meldolesi, *Nat. Rev. Neurosci.* **2005**, *6*, 626.
[11] M. Zonta, M. C. Angulo, S. Gobbo, B. Rosengarten, K.-A. Hossmann, T. Pozzan, G. Carmignoto, *Nat. Neurosci.* **2003**, *6*, 43.
[12] S. J. Mulligan, B. A. MacVicar, *Nature* **2004**, *431*, 195.
[13] N. J. Abbott, L. Rönnbäck, E. Hansson, *Nat. Rev. Neurosci.* **2006**, *7*, 41.
[14] T. Takano, G.-F. Tian, W. Peng, N. Lou, W. Libionka, X. Han, M. Nedergaard, *Nat. Neurosci.* **2006**, *9*, 260.
[15] C. Nolte, M. Matyash, T. Pivneva, C. G. Schipke, C. Ohlemeyer, U.-K. Hanisch, F. Kirchhoff, H. Kettenmann, *Glia* **2001**, *33*, 72.
[16] A. Nimmerjahn, F. Kirchhoff, J. N. Kerr, F. Helmchen, *Nat. Methods* **2004**, *1*, 31.
[17] K. A. Kasischke, H. D. Vishwasrao, P. J. Fisher, W. R. Zipfel, W. W. Webb, *Science* **2004**, *305*, 99.
[18] P. J. Campagnola, L. M. Loew, *Nat. Biotechnol.* **2003**, *21*, 1356.
[19] D. A. Dombeck, L. Sacconi, M. Blanchard-Desce, W. W. Webb, *J. Neurophysiol.* **2005**, *94*, 3628.
[20] J. Squier, M. Muller, G. Brakenhoff, K. R. Wilson, *Opt. Express* **1998**, *3*, 315.
[21] D. Yelin, Y. Silberberg, *Opt. Express* **1999**, *5*, 169.

[22] D. A. Sidorov-Biryukov, A. N. Naumov, S. O. Konorov, A. B. Fedotov, A. M. Zheltikov, *Quantum Electron.* **2000**, *30*, 1080.
[23] D. Débarre, W. Supatto, A.-M. Pena, A. Fabre, T. Tordjmann, L. Combettes, M.-C. Schanne-Klein, E. Beaurepaire, *Nat. Methods* **2006**, *3*, 47.
[24] C. W. Freudiger, W. Min, B. G. Saar, S. Lu, G. R. Holtom, C. He, J. C. Tsai, J. X. Kang, X. S. Xie, *Science* **2008**, *322*, 1857.
[25] B. G. Saar, C. W. Freudiger, J. Reichman, C. M. Stanley, G. R. Holtom, X. S. Xie, *Science* **2010**, *330*, 1368.
[26] S. Witte, A. Negrean, J. C. Lodder, C. P. J. de Kock, G. T. Silva, H. D. Mansvelder, M. L. Groot, *Proc. Natl. Acad. Sci.* **2011**, *108*, 5970.
[27] L. V. Doronina-Amitonova, A. A. Lanin, O. I. Ivashkina, M. A. Zots, A. B. Fedotov, K. V. Anokhin, A. M. Zheltikov, *Appl. Phys. Lett.* **2011**, *99*, 231109.
[28] L. V. Doronina-Amitonova, A. A. Lanin, I. V. Fedotov, O. I. Ivashkina, M. A. Zots, A. B. Fedotov, K. V. Anokhin, A. M. Zheltikov, *Appl. Phys. Lett.* **2013**, *103*, 093701.
[29] C. Eggeling, C. Ringemann, R. Medda, G. Schwarzmann, K. Sandhoff, S. Polyakova, V. N. Belov, B. Hein, C. von Middendorff, A. Schönle, S. W. Hell, *Nature* **2009**, *457*, 1159.
[30] S. W. Hell, *Nat. Methods* **2008**, *6*, 24.
[31] M. R. Freeman, *Science* **2010**, *330*, 774.
[32] S.-W. Lee, W. J. Kim, Y. K. Choi, H. S. Song, M. J. Son, I. H. Gelman, Y.-J. Kim, K.-W. Kim, *Nat. Med.* **2003**, *9*, 900.
[33] R. Cecchelli, V. Berezowski, S. Lundquist, M. Culot, M. Renftel, M.-P. Dehouck, L. Fenart, *Nat. Rev. Drug Discov.* **2007**, *6*, 650.
[34] A. A. Voronin, A. M. Zheltikov, *Phys. Rev. E* **2010**, *81*, 051918.
[35] A. A. Voronin, I. V. Fedotov, L. V. Doronina-Amitonova, O. I. Ivashkina, M. A. Zots, A. B. Fedotov, K. V. Anokhin, A. M. Zheltikov, *Opt. Lett.* **2011**, *36*, 508.
[36] Y. Fu, H. Wang, R. Shi, J.-X. Cheng, *Biophys. J.* **2007**, *92*, 3251.
[37] M. E. Matlashov, Y. A. Bogdanova, G. V. Ermakova, N. M. Mishina, Y. G. Ermakova, E. S. Nikitin, P. M. Balaban, S. Okabe, S. Lukyanov, G. Enikolopov, A. G. Zaraisky, V. V. Belousov, *Biochim. Biophys. Acta* **2015**, *1850*, 2318.
[38] B. Steinhorn, A. Sorrentino, S. Badole, Y. Bogdanova, V. Belousov, T. Michel, *Nat. Commun.* **2018**, *9*, 4044.

SUPPORTING INFORMATION

Additional supporting information may be found online in the Supporting Information section at the end of this article.

How to cite this article: Lanin AA, Pochechuev MS, Chebotarev AS, Kelmanson IV, Belousov VV, Zheltikov AM. Nonlinear-optical stain-free stereoimaging of astrocytes and gliovascular interfaces. *J. Biophotonics*. 2019;e201800432. https://doi.org/10.1002/jbio.201800432